JPE 18-4-17

https://doi.org/10.6113/JPE.2018.18.4.1140
ISSN(Print): 1598-2092 / ISSN(Online): 2093-4718

Controllable Harmonic Generating Method for Harmonic Impedance Measurement of Traction Power Supply Systems Based on Phase Shifted PWM

Qiujiang Liu*, Mingli Wu†, Jing Li*, and Junqi Zhang*

†,*School of Electrical Engineering, Beijing Jiao University, Beijing, China

Abstract

The harmonic impedance characteristic of a traction power supply system (TPSS) is necessary for taking actions to suppress the high-order harmonic resonances caused by AC electric locomotives. This paper proposes a controllable harmonic generating method (CHGM) for measuring the TPSS harmonic impedance by injecting harmonic disturbances of different frequencies and amplitudes into the TPSS. This method applies phase shifted pulse-width modulation (PSPWM) and ensures that the undesired sideband harmonics can be negligible while the desired harmonic is both controllable and adjustable. Multiple harmonics can be emitted at the same time. The implementation of the method is also presented. Simulations are carried out to validate the performance of the proposed method. Finally, experimental results on a 5 H-bridge converters platform verified the effectiveness and feasibility of the proposed method.

Key words: Harmonic analysis, Harmonic impedance, PSPWM, Railway, Resonance, Traction power supply system

I. INTRODUCTION

Distributed and complex traction power supply systems (TPSSs) draw electricity from power systems to provide single phase electricity for high-speed electric multiple units (EMUs) and ac-driven electric locomotives. Pulse-width modulation (PWM) technology and four-quadrant converters (4QCs) are now widely applied in these AC electric locomotives. When compared with the diode or thyristor rectifiers used in traditional DC electric locomotives, the AC electric locomotives generate less low-order harmonics but relatively more high-order harmonics. These high-order harmonics have led to many resonance-related accidents in China, as shown in Table I [1], [2]. Once high-order harmonic resonance occurs, the harmonic voltage and current at the resonance frequency are amplified and stimulate various problems [2]-[4]. These problems include the erroneous operation of protective devices, interference in adjacent communication lines, supply voltage distortion, and so on. In some severe cases, TPSS devices (e.g., auxiliary circuits and voltage arresters) are punctured due to resonant overvoltage. Harmonic voltage distortion in TPSSs can also cause critical power quality issues in power systems.

The high-order harmonic resonance-related accidents presented above are caused by system harmonic impedance mismatch which is related to both AC electric locomotives and traction networks. The harmonic impedance characteristic of a TPSS (TPSS-HIC) describes the harmonic impedance amplitude at different frequencies. Obtaining knowledge of a TPSS-HIC is beneficial to take effective measures to suppress the high-order resonance and to improve the TPSS power quality. For example, passive high-pass filters can be installed along the railways served as pathways for high-order harmonics. The choices of filter types and parameters are heavily dependent on the TPSS-HIC. In addition, the optimizing electrical parameters [5] and control methods [1], [6], [7] of traction converters based on the TPSS-HIC are alternative solutions for the suppression of resonance-related

Manuscript received May 4, 2017; accepted Mar. 3, 2018
Recommended for publication by Associate Editor Sung-Jin Choi.
†Corresponding Author: mlwu@bjtu.edu.cn
Tel: +0086-10-51688578, Fax: +0086-10-51687101, Beijing Jiaotong University
*School of Electrical Engineering, Beijing Jiaotong University, China

TABLE I
RESONANCE-RELATED ACCIDENTS ON CHINESE RAILWAYS

Time	Locations
Jul. 2007	Jixiannan substation of Beijing-Harbin railway
Dec. 2008	Longcheng-Changanji section of Hefei-Wuhan line
Apr. 2009	Changanji-Hefeixi section of Hefei-Wuhan line
Mar. 2010	Macheng-Wuhan section in Hubei province
Jan. 2011	Guangzhou traction substation in Guangdong
May 2011	Dahushan substations in Liaoning province
Dec. 2011	Shanhaiguan station in Hebei province
Mar. 2013	Junliangcheng substation of Beijing-Tianjin line
Dec. 2013	Xiangtang-Jiujiangxi section in Jiangxi province
Nov. 2014	Wulipu substation in Tianjin Municipality

accidents. Current research on the TPSS-HIC mainly focus on modelling and calculations [8]-[10]. The modal analysis method and the multi-conductor transmission line (MTL) theory are commonly utilized to qualitatively describe the general rules of the TPSS-HIC. These studies cannot accurately calculate the TPSS-HIC, since a traction network is a multi-conductor transmission system and the electric parameters of its installation (including catenaries, feeders, return lines, traction transformers, autotransformers, rails, etc.) are complicated and influenced by the railway environment (e.g., soil and tunnel). Precise parameters are difficult to acquire. Therefore, models must be greatly simplified, especially for rails. Moreover, models and numerical calculations cannot precisely determine the power system harmonic impedance at frequencies greater than 1000 Hz, which has a great effect on the TPSS-HIC [11]. As a result, it is barely possible to quantitatively estimate the TPSS-HIC by modelling and calculation methods.

When compared with the aforementioned modelling and calculation methods, precision parameters of TPSSs are not necessary if fully controlled harmonic currents are injected into TPSSs to directly measure the harmonic impedance. In power systems, invasive methods have been developed to measure the system impedance at the point of common coupling. However, these methods are not suitable for TPSSs. In [12]-[14], the capacitor switching method and the thyristor-controlled circuit switching method are adopted to measure the power system impedance. However, the generated currents at high frequencies are uncontrollable. Thus, the measurements are not accurate if the harmonic content is not large enough. In [15], a digital-to-analog converter and a power amplifier are described for harmonic generation. However, the catenary has to be switched off to perform measurements and it does not include the high-voltage feeding network impedance. In the photovoltaic field, harmonics are injected into power systems to estimate the grid impedance which can be used for the detection of islanding operation [16]-[20]. These methods are generally designed for low frequency impedance estimation and do not cover the resonant frequencies of TPSSs. In summary, in the market, products that can generate fully controlled harmonics mainly include AC grid power modules [21], active power filters (APFs) [22] and signal generators [15]. They all have different features, but may not be suitable for TPSS-HIC measuring, as shown in Table II.

TABLE II
COMPARISON OF DIFFERENT HARMONIC GENERATORS

	AC Grid Power Module[21]	APF[22]	Signal Generator[15]	Proposed Method
Cost	High	Medium	Low	Medium
Extra Power Source	220V or 380V AC	Not Required	220V AC	No Required (If capacitors are used)
Power Rating	Medium (<100 kVA)	High (up to MVA)	Low (<200 VA)	High (up to MVA)
Voltage Rating	Low (<300 V)	High (up to kV)	Low (<300 V)	High (up to kV)
Frequency Range	Low (<1 kHz)	Low (<1 kHz)	High (up to MHz)	Medium (up to 5 kHz)
Online Test	No (TPSS has to power off)	Yes	No (TPSS has to power off)	Yes

Research on harmonic impedance measuring methods in the field of TPSSs are rarely mature. There are few studies on the harmonic generating methods used for the TPSS-HIC measuring. Hence, the aim of this paper is to explore a novel controllable harmonic generating method for measuring TPSS-HIC based on cascaded H-bridge converters (CHBCs) and phase shifted pulse-width modulation (PSPWM). Depending on this method, harmonic disturbances with various frequencies and amplitudes can be injected into TPSSs. The frequency range of the generating harmonics is wide enough to cover the frequencies of resonant accidents in order to obtain the details of the TPSS-HIC. The amplitudes of generated harmonics are controllable to increase the measurement accuracy. Online tests are available. As a result, the TPSS does not have to power off. The power rating and voltage rating are also suitable for TPSSs. A series of simulations and experiments have been developed to verify the effectiveness of the proposed method.

This remainder of this paper is organized as follows. Section II briefly describes the overall measuring mechanism of the implementation. In Section III, details of the proposed controllable harmonic generating method utilized for harmonic injection are presented with simulations. Experimental verifications are described in Section IV. Section V provides a brief summary and some conclusions.

II. HARMONIC IMPEDANCE MEASURING MECHANISM

An implementation diagram of harmonic impedance measuring is depicted in Fig. 1. It takes typical auto-transformer (AT)-fed networks as an example. However, the proposed method is suitable for all kinds of TPSSs. The all-parallel AT-fed networks include catenaries, contact wires, messenger wires, ATs, rails, protect wires and feeders. The three-phase 110/220 kV utility power is stepped down to two single-phase 2×27.5 kV feeders by a traction transformer in an electrical substation (ESS) to supply the AT networks. ATs are installed in AT posts or section posts and are distributed along tracks every 10–15 km. Trains running on tracks using PWM technology are the main harmonic sources that result in high-order harmonic resonances in TPSSs.

The harmonic generator (HG), the blue block shown in Fig. 1, is connected directly between the catenary and the rail and it is utilized to emit harmonic disturbances of various frequencies and amplitudes. The generated harmonic current i_g and harmonic voltage u_g are recorded. Then the total input impedance of the TPSS at the test position can be obtained as:

$$Z_e(f_g)=\frac{U_g(f_g)}{I_g(f_g)} \quad (1)$$

where f_g (in Hz) is the frequency of the generated harmonic disturbance. The value of f_g can vary in the range of interest to draw a plot of the impedance characteristics, i.e., amplitudes versus frequencies. When the impedance profile reaches a local maximum or minimum, the corresponding specific frequency is the resonant frequency. This method includes power system impedance information and does not require actual TPSS parameters. However, there must be no traction loads in the power supply section where the test is carried out (there are no locomotives in Fig. 1). Otherwise, the test results would contain the impedance of the traction unit input filters in addition to the TPSS.

The HG was constructed with a single-phase CHBC based on insulated gate bipolar transistors (IGBTs). It is able to generate high-order harmonic disturbances. The system can also emit inter-harmonics for decreasing the background noise influence and for increasing the measurement accuracy. The HG has good on-line test performance when it is applied to various TPSS locations and conditions. A schematic diagram of the HG is shown in Fig. 2(a), where R_1–R_N are voltage balancing resisters, U_{dc1}–U_{dcN} are DC-link sources, L_c represents the total inductance of the filter inductor and the transformer leakage impedance, u_e is the equivalent ideal power source of the TPSS, u_c is the output voltage of the CHBC, u_s is the transformer voltage of the low voltage side, i_c is the current of the CHBC, and n_t is the transformer turns ratio. If n_t is set to 1, there is no need for a transformer and the HG can be connected directly to the TPSS. Generally, the

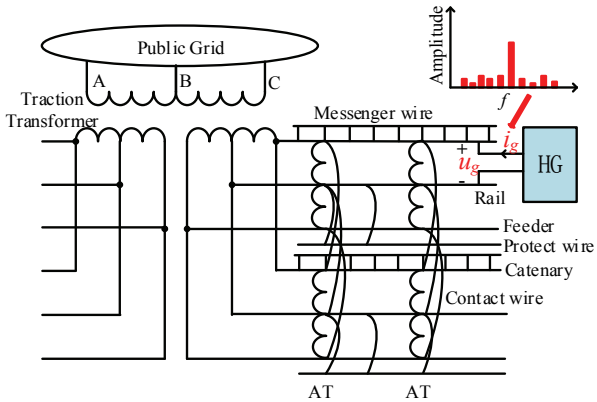

Fig. 1. Implementation diagram of the harmonic impedance measuring.

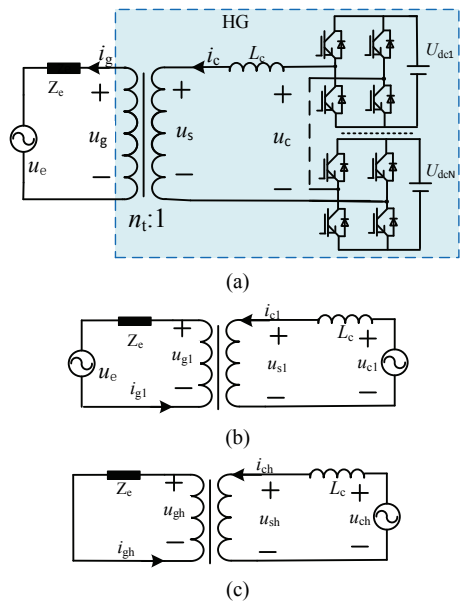

Fig. 2. HG based on cascaded H-bridge converters: (a) HG topology; (b) Fundamental equivalent circuit; (c) Harmonic equivalent circuit.

DC-link voltages of CHBCs should be supplied by separate voltage sources. Capacitors, photovoltaic cells, batteries and rectifiers with isolated links can undertake this task. Using capacitors to increase the viability of the proposed method is a feasible solution that has been verified by simulations and experiments [23]. Figs. 2(b)–(c) describe the equivalent circuits. The TPSS supplies active power to the HG as shown in Fig. 2(b). Fig. 2(c) illustrates the harmonic equivalent circuit where the TPSS serves as the harmonic load and the HG acts as the harmonic source.

III. THE PROPOSED CONTROLLABLE HARMONIC GENERATING METHOD

In order to emit harmonic disturbances in a wide range of frequencies, the system equivalent switching frequency of the HG must be sufficiently high. PSPWM [24], [25], which is

widely applied in multilevel converters, can obtain a high equivalent switching frequency with power semiconductor devices operating at relatively low switching frequencies. With respect to other modulation strategies utilized in high power and high voltage multilevel converters [26]–[29], such as the level shifted PWM (LSPWM) technique, selective harmonic elimination (SHE) modulation and space-vector modulation (SVM), PSPWM does not need complex offline computations and the switching frequency of each cell is fixed. The proposed method is based on PSPWM. PSPWM is easy to implement in digital control systems at high control frequencies, such as field programmable gate array (FPGA) based systems. If the control interval is small enough, the modulation can be regarded as a natural sampling strategy. Therefore, in this paper double-edged natural sampling modulation is considered.

A. Spectrum Analysis: The Modulating Wave Only Includes the Fundamental Comment

The PWM working principle in one H-bridge converter is shown in Fig. 3. One carrier is compared with two references π phase shifted with respect to each other. When the left arm reference u_{rl}^* is higher than the carrier, the switch S1 is on and the switch S2 is off. On the other hand, when u_{rl}^* is lower than the carrier, S1 is off and S2 is on. The right reference u_{rr}^* is compared with the carrier to generate pulses used for S3 and S4.

Bowes and Bird [30], [31] developed the most well-known double Fourier series analytical method for determining the harmonic model of a PWM-switched converter. The one arm output voltage $u_{an}(t)$ or $u_{bn}(t)$ is given by:

$$\begin{aligned} f(x,y) &= \frac{A_{00}}{2} + \sum_{n=1}^{\infty}(A_{0n}\cos ky + B_{0n}\sin ny) \\ &+ \sum_{m=1}^{\infty}(A_{m0}\cos mx + B_{m0}\sin mx) \\ &+ \sum_{m=1}^{\infty}\sum_{\substack{n=-\infty \\ (n\neq 0)}}^{\infty}[A_{mn}\cos(mx+ny) + B_{mn}\sin(mx+ny)] \end{aligned} \tag{2}$$

where A_{mn} and B_{mn} are harmonic coefficients. In order to calculate these coefficients, the two-dimensional integration method is applied which is shown in Fig. 4.

In Fig. 4, ω_o and ω_c are the angular frequency of the modulating wave and carrier wave, respectively. A straight line $y'(t)$ with a slope of ω_o/ω_c represents the relationship of the modulating and carrier wave passing through the origin in x0y plane. The outlines of the shaded areas represent the modulating wave. The straight line intersects the shaded areas resulting in periodic intersection points x_{rk} and x_{fk} given by:

$$\begin{cases} x_{rk} = 2k\pi - \dfrac{\pi}{2}(1 + M\cos y) \\ x_{fk} = 2k\pi - \dfrac{\pi}{2}(1 + M\cos y) \end{cases} \tag{3}$$

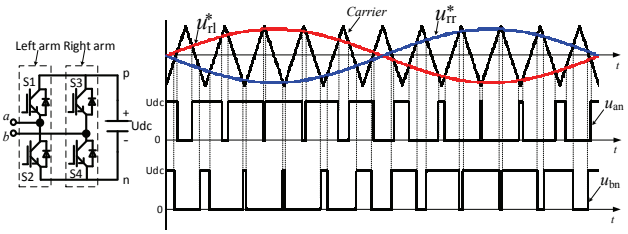

Fig. 3. PWM operating principle for one H-bridge converter.

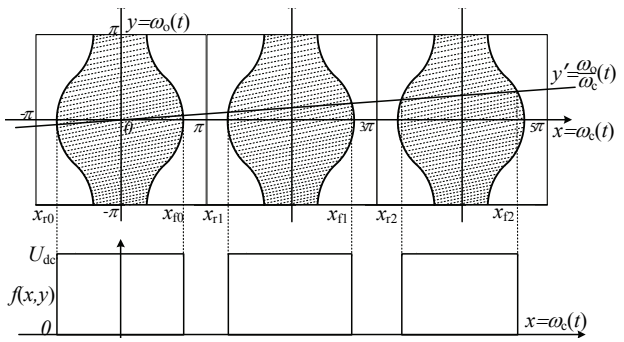

Fig. 4. Modulation model of the PWM process.

where the integer variable k (k=0,1,2,…) is the index of the periods. The resultant PWM wave is the value of the function $f(t) = f(x(t),y(t))$. At x_{rk}, $f(x,y)$ changes from 0 to U_{dc}, while at x_{fk}, $f(x,y)$ changes from U_{dc} to 0. Hence, double Fourier series coefficients can be derived by the following integral equation:

$$C_{m,n} = A_{m,n} + jB_{m,n} = \frac{1}{2\pi^2}\int_{-\pi}^{\pi}\int_{-\pi}^{\pi} f(x,y)e^{j(mx+ny)}dxdy \tag{4}$$

where:

$$\begin{cases} y(t) = \omega_o t + \theta_o \\ x(t) = \omega_c t + \theta_c \end{cases} \tag{5}$$

where θ_o and θ_c are the initial phase of the fundamental modulating and carrier wave. In Fig. 4, phases are set as 0 to simplify the analysis. Based on equations (2), (4) and (5), the output voltage of one arm $u_{an}(t)$ can be obtained [30]. The H-bridge converter output voltage u_{ab}(t) is the difference between the left and right arm and is shown as:

$$u_{ab}(t) = u_{an}(t) - u_{bn}(t)\,. \tag{6}$$

Assuming that θ_c=0, the left arm θ_o=0 and the right arm θ_o=–π, u_{ab}(t) can be expressed as:

$$\begin{aligned} u_{ab}(t) &= f(\omega_c t, \omega_o t) - f(\omega_c t, \omega_o t - \pi) \\ &= U_{dc}M\cos(\omega_o t) \\ &+ \frac{4U_{dc}}{\pi}\left\{\sum_{m=1}^{\infty}\sum_{k=-\infty}^{\infty}\frac{1}{2m}J_{2k-1}(m\pi M)\cos[(m+k-1)\pi]\right\} \\ &\quad \cos[2m\omega_c t + (2k-1)\omega_o t] \end{aligned} \tag{7}$$

where m is the carrier harmonic index, n is the sideband harmonic index, M is the modulation depth, and $J_n(x)$ is the nth-order Bessel function:

$$J_n(x) = \frac{1}{2\pi}\int_{-\pi}^{\pi} e^{-jx\cos y}e^{jny}dy\,. \tag{8}$$

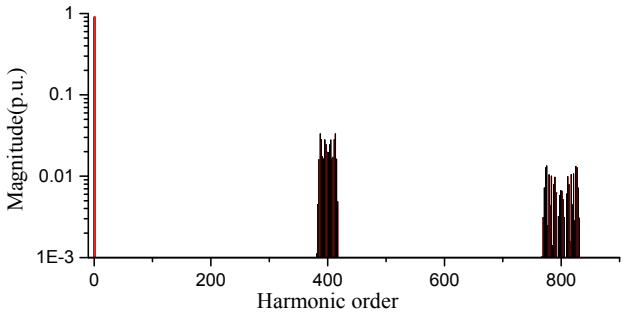

Fig. 5. The spectrum of the CHBC output voltage when the modulating wave only includes a fundamental component.

Considering that the CHBC is constructed with N cells and that the carrier phase-shift angle is π/N between each cell, the output voltage of the CHBC is given by [32]:

$$\begin{aligned} u_{\mathrm{c}}(t) &= \sum_{i=1}^{N} u_{\mathrm{ab}i} \\ &= NU_{\mathrm{dc}}M\cos(\omega_{\mathrm{o}}t) \\ &+ \frac{4U_{\mathrm{dc}}}{\pi}\left\{\begin{array}{l}\sum\limits_{m=1}^{\infty}\sum\limits_{n=-\infty}^{\infty}\frac{1}{2m}J_{2n-1}(Nm\pi M) \\ \cos[(Nm+n-1)\pi]\cos[2mN\omega_{\mathrm{c}}t+(2n-1)\omega_{\mathrm{o}}t]\end{array}\right\} \end{aligned} \tag{9}$$

where the DC voltages of each cell are assumed to be identical. Figure 5 describes the analysis result based on equation (9) where M=0.9, ω_{o}=100π rad/s, ω_{c}=4000 π rad/s, N=5.

Equation (9) and Fig. 5 indicate that the lowest carrier harmonic frequency is $2Nf_{\mathrm{c}}$ and that the output voltage harmonics mainly include odd order sideband harmonics around the $2mN$th- order carrier harmonics.

B. Spectrum of PSPWM: The Modulating Wave Includes both Fundamental and Harmonic Comments

Section III-A presents the harmonic spectrum analysis method focusing on a single sinusoidal modulating wave. When harmonics are injected into TPSSs to measure the harmonic impedance, the modulating wave includes the fundamental component and the harmonic component whose frequency range must be wide enough to cover the resonant frequencies. In [33], [34], a theoretical analysis of the harmonic spectra is reported when multiple modulation frequencies are used. However, in these papers, only a single phase converter leg is addressed. There are hardly any studies on the theoretical spectrum analysis of PSPWM based on the CHBC. Nevertheless, it is important to analyze the harmonic spectra of PSPWM since this helps when it comes to designing the parameters and understanding the performance of the impedance measuring system. Therefore, in this section a theoretical analysis of an N-cell CHBC output voltage is presented depending on double Fourier series method. When G harmonics are injected into TPSSs, the total modulating wave can be expressed as:

$$u_{\mathrm{r}}^{*} = M\cos(\omega_{\mathrm{o}}t) + \sum_{k=1}^{G} M_k\cos(h_k\omega_{\mathrm{o}}t) \tag{10}$$

where M_k and h_k are the modulation depth and harmonic order of the kth harmonic, respectively. The double Fourier series coefficients can be calculated by:

$$\begin{aligned} C_{m,n}(h_1,h_2\ldots h_G) &= \frac{1}{2\pi^2}\int_{-\pi}^{\pi}\int_{-\pi}^{\pi} U_{\mathrm{dc}}e^{j(mx+ny)}dxdy \\ &= \frac{U_{\mathrm{dc}}}{2\pi^2}\int_{-\pi}^{\pi}\int_{-\frac{\pi}{2}[1+M\cos(\omega_{\mathrm{o}}t)+\sum_{k=1}^{G}M_k\cos(h_k\omega_{\mathrm{o}}t)]}^{\frac{\pi}{2}[1+M\cos(\omega_{\mathrm{o}}t)+\sum_{k=1}^{G}M_k\cos(h_k\omega_{\mathrm{o}}t)]} e^{j(mx+ny)}dxdy . \end{aligned} \tag{11}$$

In order to simplify the analysis process, only one harmonic is considered in this section. A general coefficients solution for emitting G harmonics is described in Appendix B. Thus, equation (11) is reduced to equation (12):

$$C_{m,n}(h_1) = \frac{U_{\mathrm{dc}}}{2\pi^2}\int_{-\pi}^{\pi}\int_{-\frac{\pi}{2}(1+M\cos y+M_1\cos h_1 y)}^{\frac{\pi}{2}(1+M\cos y+M_1\cos h_1 y)} e^{j(mx+ny)}dxdy . \tag{12}$$

By calculating $C_{m,n}(h_1)$, the output voltage of a single phase converter arm with both fundamental and harmonic modulating waves is given by:

$$\begin{aligned} u_{\mathrm{an}} &= U_{\mathrm{dc}} + \frac{MU_{\mathrm{dc}}}{2}\cos(\omega_{\mathrm{o}}t) + \frac{M_1U_{\mathrm{dc}}}{2}\cos(h_1\omega_{\mathrm{o}}t) \\ &+ \sum_{m=1}^{\infty}\sum_{n=-\infty}^{\infty} C_{m,n}(h_1)\cos[m(\omega_{\mathrm{c}}t+\theta_{\mathrm{c}}) + n(\omega_{\mathrm{o}}t+\theta_{\mathrm{o}})] \end{aligned} \tag{13}$$

where $C_{m,n}(h_1)$ is expressed as:

$$\begin{aligned} C_{m,n}(h_1) &= \frac{2U_{\mathrm{dc}}}{m\pi}J_0(m\frac{\pi}{2}M_1)J_k(m\frac{\pi}{2}M)\sin[(m+k)\frac{\pi}{2}]|_{k=|n|} \\ &+ \frac{2U_{\mathrm{dc}}}{m\pi}J_0(m\frac{\pi}{2}M)J_{d_1}(m\frac{\pi}{2}M_1)\sin[(m+d_1)\frac{\pi}{2}]|_{h_kd_1=|n|} \\ &+ \frac{2U_{\mathrm{dc}}}{m\pi}\left\{\begin{array}{l}\sum J_k(m\frac{\pi}{2}M)J_{d_1}(m\frac{\pi}{2}M_1) \\ \sin[(m+k+d_1)\frac{\pi}{2}]|_{\pm k\pm h_kd_1=|n|}\end{array}\right\} . \end{aligned} \tag{14}$$

Then like the derivation process of equation (7), the H-bridge converter output voltage can be obtained from equations (13)–(14). Considering that the cascaded number of the CHBC is N, the ultimate output voltage of the CHBC is given by:

$$\begin{aligned} u_{\mathrm{c}}(t) &= MNU_{\mathrm{dc}}\cos(\omega_{\mathrm{o}}t) + M_1NU_{\mathrm{dc}}\cos(h_1\omega_{\mathrm{o}}t) \\ &+ \left\{\begin{array}{l}2\sum\limits_{m=1}^{\infty}\sum\limits_{n=-\infty}^{\infty}C_{m,2n-1}(h_1)(\sum\limits_{i=1}^{N}\cos\frac{m(i-1)\pi}{N})\cos(m\omega_{\mathrm{c}}t+(2n-1)\omega_{\mathrm{o}}t) \\ -2\sum\limits_{m=1}^{\infty}\sum\limits_{n=-\infty}^{\infty}C_{m,2n-1}(h_1)(\sum\limits_{i=1}^{N}\sin\frac{m(i-1)\pi}{N})\sin(m\omega_{\mathrm{c}}t+(2n-1)\omega_{\mathrm{o}}t)\end{array}\right\} . \end{aligned} \tag{15}$$

The calculation details of equations (13)–(15) are presented in Appendix A. A graphical representation of the harmonic spectrum is provided in Fig. 6 adopting equation (15) by programming in an m-file. This is compared with FFT analysis result using MATLAB/Simulink. From Fig. 6, it can be seen that the theoretical analysis agrees with the simulation result. The difference is mainly introduced by utilizing limited m and n in the program while they are infinite in practice. However, the difference is smaller than 0.0004 p.u., which is negligible. Therefore, in the following section, equation (15) is used as a guide to design the controllable harmonic generating method.

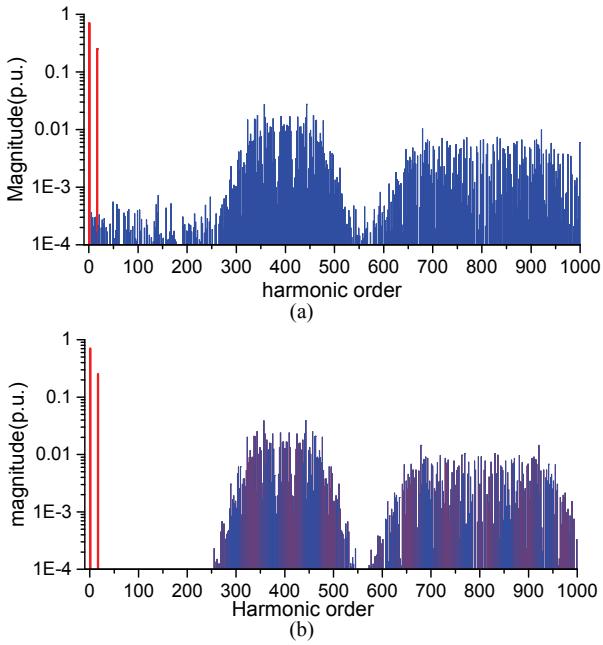

Fig. 6. Output voltage spectra of the CHBC with M=0.7, M_1=0.25, f_o=50 Hz, N=5 and h_1=17: (a) FFT analysis result using MATLAB; (b) Calculation result using equation (15).

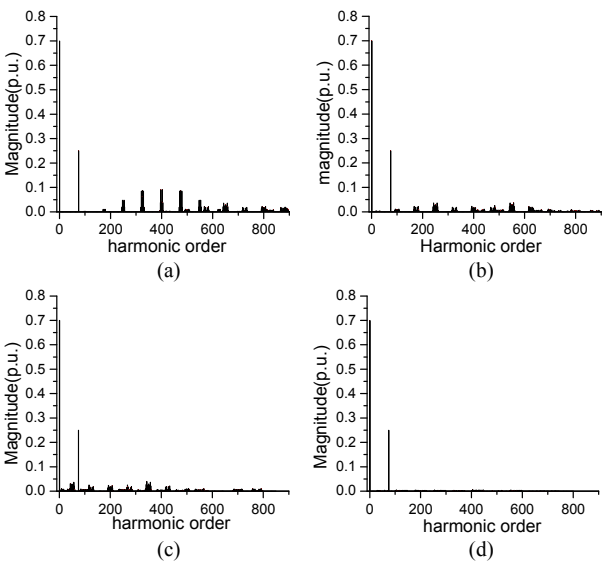

Fig. 7. Harmonic spectra of the CHBC with different N and f_c with f_o=50 Hz, h_1=67, M=0.7, M_1=0.25: (a) N=2, f_c=5000 Hz; (b) N=4, f_c=2500 Hz; (c) N=8, f_c=1250 Hz; (d) N=10, f_c=500 Hz.

C. Design and Implementation of The Controllable Harmonic Generating Method

When no harmonic disturbance is desired, the modulating wave should only include the fundamental component. The harmonic distribution of the CHBC output voltage is depicted in Fig. 5, where the first group of sideband harmonics is around the frequency $2Nf_c$. When a desired harmonic current at a specific frequency is injected into the TPSS, the sideband harmonics may also fall into the resonant frequency range.

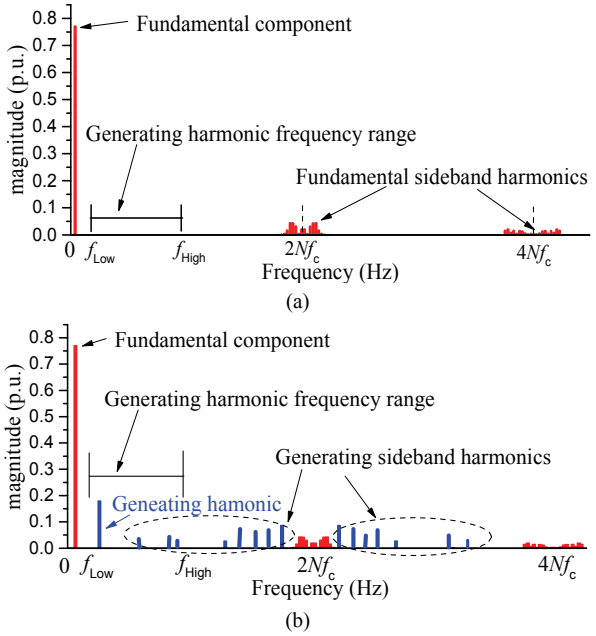

Fig. 8. Harmonic spectrum schematic diagram: (a) Before a desired harmonic is generated; (b) After a specific harmonic is injected.

This condition has a negative effect on generating a pure harmonic. Therefore, the sideband harmonic components should be as small as possible to increase the measuring precision. Equation (15) indicates that the harmonic spectrum is related to the cascaded number N and the switching frequency f_c. In other words, even if the total equivalent switching frequency of the HG is the same, the harmonic spectra are discrepant when different values of N and f_c are adopted. For example, as shown in Fig. 7, $2Nf_c$ is set as 20 kHz in all of the subplots. However, the sideband harmonic distributions are different. In terms of suppressing the sideband harmonics it is beneficial to employ a higher cascaded number N and f_c. However, this increases both the cost and complexity of the HG system. In practice, a tradeoff decision must be made.

The following steps are listed to describe the proposed controllable harmonic generating method (CHGM) for generating desired harmonics.

1) Decide the frequency limits of generating the harmonics represented by from f_{Low} to f_{High}.
2) Set the value $2Nf_c$ as at least two or three times higher than f_{High}. This ensures that the sideband harmonics of the fundamental modulating wave are moved out of the frequency range determined in Step 1, as shown in Fig. 8(a).
3) Design proper N and f_c depending on equation (15) to guarantee that most of the sideband harmonics are out of the desired frequency range and that the small part of the sideband harmonics falling in the addressed frequency range is ignorable.

4) Synthesize the ultimate modulating wave including the fundamental and harmonic components. Then the drive pulses are generated and sent to each power switch via PSPWM. Finally, the controllable and pure harmonic disturbances are injected into the TPSSs.

Fig. 9 illustrates the whole control scheme designed for the HG described in Fig. 2(a). A full implementation of the proposed CHGM has been developed. In Fig. 9, U_{dc}^{*} is the cell DC voltage reference; u_{dck} is the actual DC voltage of the kth cell; u_{ravek}^{*} is the modulating wave for balancing the DC voltage of each cell when individual capacitors are adopted; w(s) is the current control regulator; u_{rh}^{*} is the harmonic modulating wave; and u_{r}^{*} is the total modulating wave including both fundamental and harmonic components. The fundamental power control (FPC), corresponding to Fig. 2(b), is utilized to regulate the active fundamental power for compensating the HG losses and for balancing the cell DC-link voltage.

In the FPC scheme, a regulator, i.e. a proportional and integral (PI) regulator, is utilized to regulate the total voltage of the DC capacitors to a desired reference value. This slow-voltage-loop regulator output synchronized with the input voltage phase by a single-phase phase locked loop (PLL) makes the AC current reference. An inner-current-loop is regulated by a proportional resonant (PR) controller. The PR controller is independent from the system parameters and uses the grid frequency as the resonant frequency. With proper coefficients, the current control result theoretically has a zero steady-state error and a good dynamic performance. Grid voltage u_s is added to the output of the current loop to suppress grid voltage disturbances. The DC-link voltage balancing of each cell is important. In this paper, the individual voltage balancing control method [35], [36] is adopted.

In the CHGM, as shown in the red part in Fig. 9, a PI controller is required to regulate the harmonic voltage generated by this converter to the harmonic voltage amplitude reference. A Fast Fourier Transform (FFT) is adopted to calculate the practical amplitude of the generating harmonic. The FFT algorithm can be implemented in a FPGA chip to reduce the calculation time. The output of the PI controller and the harmonic angular frequency reference ω_{h}^{*} synthesize the desired harmonic modulating wave. The ON/OFF instruction enables/disables the harmonic generating. Then the total modulating wave u_{r}^{*} is modulated by PSPWM to generate pulses and drive power switches. The CHGM corresponds to Fig. 2(c).

A PSCAD/EMTDC model was developed to verify the proposed harmonic generating method. The model is the same as that shown in Fig. 2(a). In this model, u_e is set to 27.5 kV and the DC voltage reference of each cell is 500 V. The ideal transformer ratio is 10:1. L_c is 2 mH. The switching frequencies of the IGBTs are 1000 Hz and the cell number is 10.

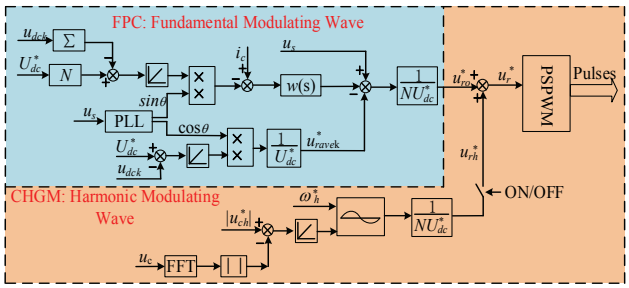

Fig. 9. Control block diagram of the proposed method.

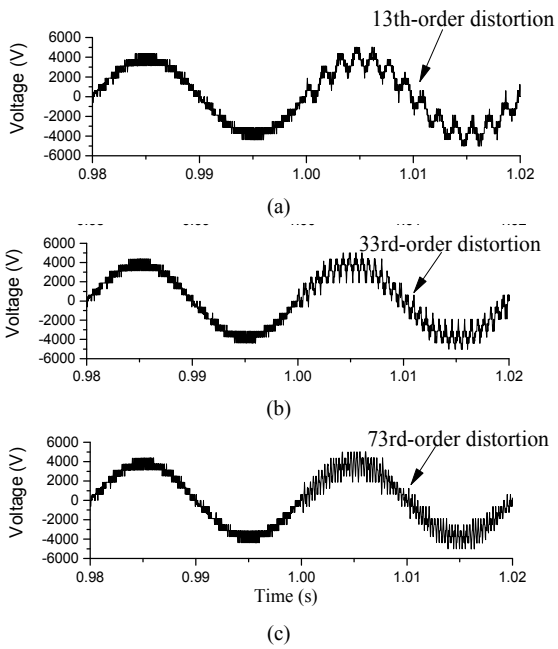

Fig. 10. CHBC output voltages generating: (a) 13th-order harmonic; (b) 33rd-order harmonic; (c) 73rd-order harmonic.

Three simulation cases were given to describe the performances of the control method. The first case was to emit a 13th-order harmonic (low frequency) disturbance, the second case was a 33rd-order (middle frequency) disturbance and the third case was a 73rd-order (high frequency) disturbance. As depicted in Fig. 10, before 1 s, the harmonic emitting instruction was not given, and the HG worked as a rectifier with a power factor approaching 1. The multilevel waveform of u_c was obvious. After 1 s, the HG emitted a 1000 V harmonic voltage. As a result, the output voltage of the CHBC became distorted with harmonic gaps. The higher the frequency of the generating harmonic, the denser the disturbances added to the main multilevel output voltage became. However, the fundamental components of the three output voltage waveforms were nearly the same since they worked for absorbing active power for the HG.

Output harmonic voltages result in harmonic currents of the same frequencies as represented in Fig. 11, where the red curve shows the fundamental component of the output current and the black waveforms are the actual total currents. Before

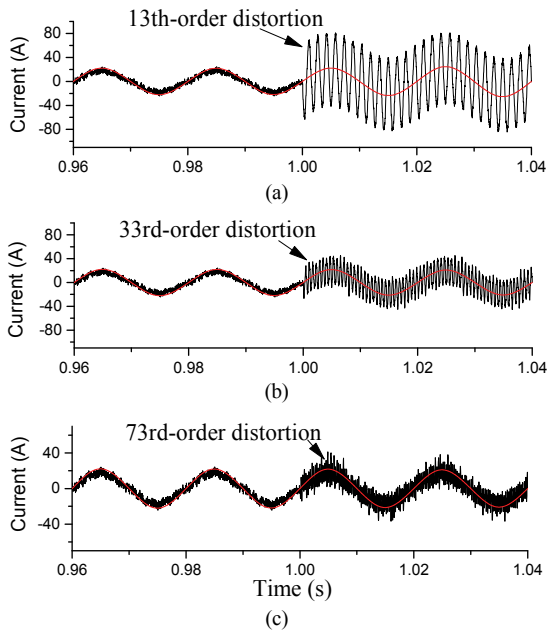

Fig. 11. HG currents generating: (a) 13th-order harmonic; (b) 33rd-order harmonic; (c) 73rd-order harmonic.

1 s, the HG worked as a unity-power factor rectifier. Therefore, the current only had a little harmonics, which was nearly a sine wave. After 1 s, a lot of harmonic currents were superposed on the fundamental current component. In subplots (a), (b) and (c), the harmonic currents are the 13th-order, 33rd-order and 73rd-order harmonic currents, respectively. The impedance is larger at a higher frequency. Therefore, the harmonic current amplitude decreases in turn in the three subplots under the same harmonic voltage stimulation.

IV. Experimental Verification

The CHGM was further validated on an experimental prototype. Based on the test data of resonant accidents and previous studies [1], the resonant frequency range is generally from 750 Hz to 3750 Hz. Therefore, the generating harmonic frequency is set from 500 Hz to 4000 Hz which covers the actual resonant frequencies. The experimental prototype consists of 5 H-bridge converters, as shown in Fig. 12(a), controlled by a DSP+FPGA control board. The DSP (TMS320C6748, Texas Instruments Inc.) is responsible for the control algorithm calculating in the discrete-time domain and for obtaining the modulating wave. The FPGA (XC6SLX45, Xilinx Inc.) is utilized to implement the PSPWM. The drive pulses are sent to each of the converters via optical fibers. The control board receives harmonic generating instructions ON/OFF from the operating software installed in a host PC through UDP communication. The DC-link voltage for each of the H-bridge converters is maintained at 28 V and the switching frequencies of IGBTs are 2000 Hz. As a result, the total equivalent switching

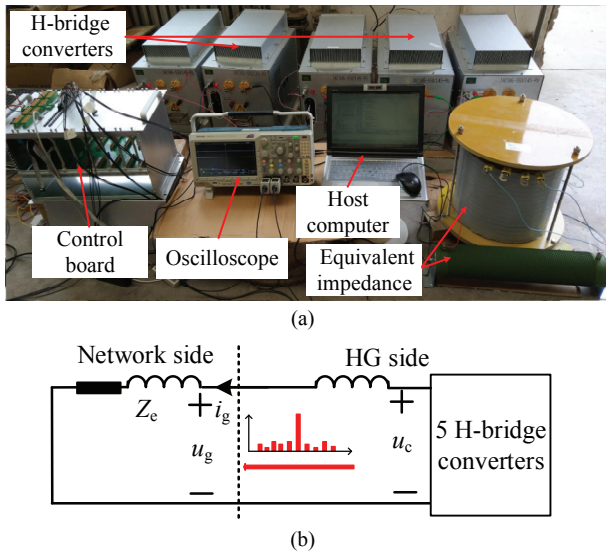

Fig. 12. Laboratory prototype: (a) A photo of the actual experimental system; (b) Equivalent harmonic circuit when harmonics are generating.

frequency $2Nf_c$ is 20 kHz. The equivalent impedance circuit of the network side consists of one 50 Ω resister and one 3 mH reactor.

Two cases were carried out to verify the performance of the CHGM. In the first case, harmonics at different single frequencies are generated. As shown in Fig. 13(a), before the harmonic generating instruction was given, the modulating wave only included the fundamental component. The profile of the CHBC output voltage u_c is multilevel and the current i_g is nearly sinusoidal. The FFT analysis result for u_c shows that the 50 Hz component occupies the main part and that the harmonics mainly appear at around 20 kHz and 40 kHz and so on. This result corresponds with equation (9) and Fig. 5. The fundamental voltage of u_c is 72 V and the maximum harmonic voltage is less 2.8 V, which accounts about 2.0% of the total equivalent DC-link voltage. Fig. 13(b) shows experimental result of the output voltage spectrum when 20 V harmonic at 850 Hz is desired. When compared to Fig. 13(a), a lot of distortion was added to the output voltage u_c. The network current i_g contains a lot of harmonic current components at the same frequency. A FFT analysis of CH1 shows that the 850 Hz harmonic is about 20 V, which accounts 14.3% of NU_{dc}=140 V. The maximum sideband harmonic is less than 2.3% of NU_{dc}, and it appears at about 17.9 kHz in the first sideband harmonic group.

Fig. 13(c) and Fig. 13(d) show that 2500 Hz and 3350 Hz harmonic were generated, respectively. Since the generating harmonic frequencies are higher than 850 Hz, the distortions of u_c and i_g are much denser than those in Fig. 13(b). The amplitudes of the specific generating harmonics were set to about 20 V in Figs. 13(c)–(d). It should be noted that the harmonic spectra of u_c in Figs. 13(c)–(d) are different from those in Fig. 13(a) and Fig. 13(b). The harmonics are spread

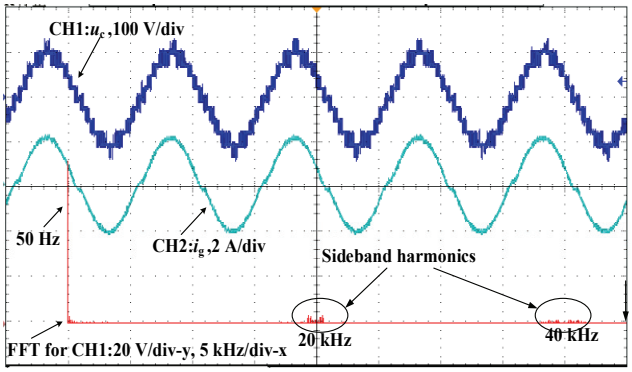

(a)

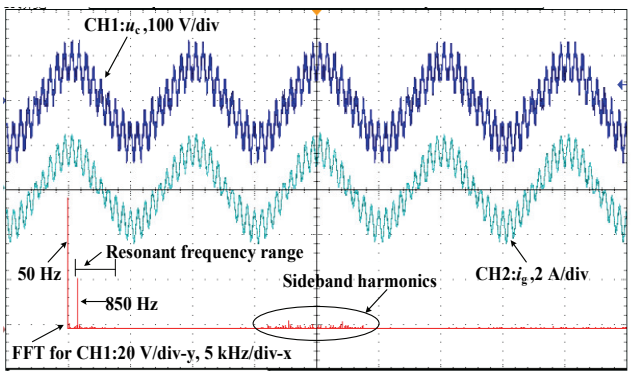

(b)

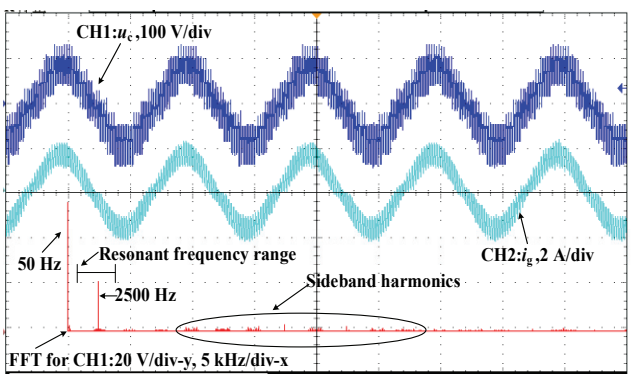

(c)

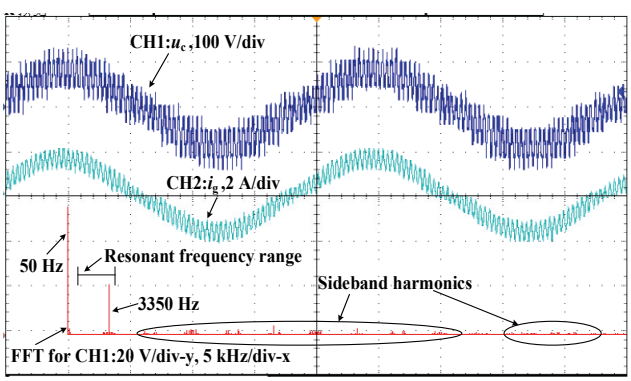

(d)

Fig. 13. Experimental results of generating a single harmonic: (a) The harmonic generating instruction was not sent; (b) Generation of an 850 Hz harmonic; (c) Generation of a 2500 Hz harmonic; (d) Generation of a 3350 Hz harmonic.

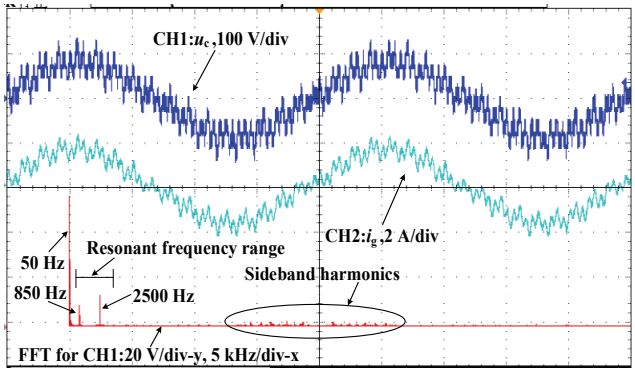

(a)

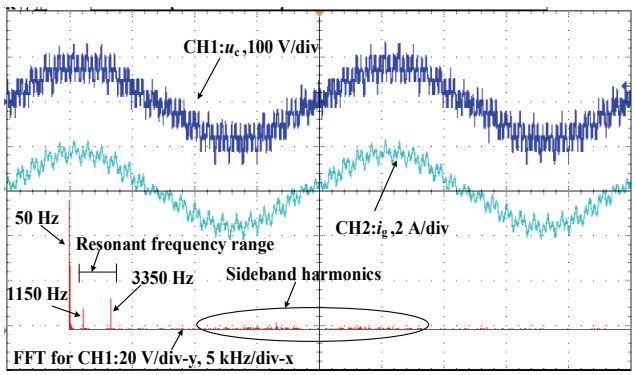

(b)

Fig. 14. Experimental results of generating harmonics at two different frequencies at the same time: (a) Generating 850 Hz and 2500 Hz harmonics; (b) Generating 1150 Hz and 3350 Hz harmonics.

around the integral multiple frequencies of $2Nf_c$, and at other frequencies. These results show good agreement with equation (15).

Several other factors are also responsible for these results. This is inescapable in actual physical implementation systems. In this paper, the control interval is set to 50 μs which is equal to $1/(2Nf_c)$. A smaller control interval is beneficial for decreasing the discretization error introduced by the control system and for improving the output voltage harmonic performance. However, it also increases the computation cost. Furthermore, the influence of the dead time caused by power switches is included [37], [38], especially when the generating harmonic frequency is high. In the experimental physical implementation of this paper, the dead times of the IGBTs are set as 1.5 μs. Other elements also have negative effects on the output voltage harmonic spectrum, such as the DC-link voltage fluctuations of H-bridge converters [32], [39], and the drop voltage difference of power switches. However, although these negative factors exist in actual experimental systems, the harmonics falling in the resonant frequency range are very small except for the desired ones, as shown in Figs. 13(b)-(d).

In the second case, harmonics at two different frequencies were generated at the same time as presented in Fig. 14. In Fig. 14(a), the harmonic frequencies are 850 Hz and 2500 Hz. Their amplitudes are 8 V and 12 V, respectively. In Fig. 14(b), the harmonic frequencies are 1150 Hz and 3350 Hz, and their amplitudes are also 8 V and 12 V, respectively. In Fig. 14(a) and Fig. 14(b), the desired harmonic at the lower frequency accounts for 5.7% of the equivalent total DC-link voltage 140 V and the higher frequency harmonic is about 8.6%. In order to avoid overmodulation, the amplitude for each of the generating harmonics in Fig. 14 is set to be smaller than those in Fig. 13. From Figs. 14(a) and 14(b), it can be seen that the distortions of u_c and i_g are different from those in Fig. 13. In Fig. 14, two obvious harmonic peaks were added onto the i_g waveform, which represents the two specific generating harmonics. Meanwhile in Fig. 13 only one harmonic peak was added to the fundamental component of i_g.

Hence, all of the experimental results verify that pure harmonics with controllable frequencies and amplitudes have been injected into the network side in the resonant frequency range. Then the harmonic impedances of TPSSs at different frequencies can be measured based on equation (1).

V. Conclusions

In this paper, a controllable harmonic generating method has been proposed to measure the harmonic impedance of TPSSs. The proposed method is based on the PSPWM that is widely applied in multilevel converters. With proper designing of the carrier frequency and the CHBC number, undesired sideband harmonics can be moved out of the resonant frequency range while the desired specific pure harmonic is both controllable and adjustable. As a result, the harmonic impedance can be accurately measure. The proposed method is fully verified with a closed loop controller in a simulation model. Furthermore, experiments have been carried out with an 11-level prototype that consists of 5 H-bridge converters and a DSP+FPGA control board. Experimental results demonstrated the validity of the proposed method.

When this method is implemented in an actually-scaled high power system, some factors should be considered fully to obtain good applicability, including DC voltage fluctuations, control intervals, dead time, electromagnetic compatibility, constructing complexity and portability. These issues will be the emphasis of future research.

Appendix A

Spectrum Theoretical Calculation of PSPWM for Harmonic Generation

When m=0 and n=0, the calculation result of equation (12) represents the DC bias coefficient which is given by:

$$C_{0,0}(h_1) = U_{\mathrm{dc}}. \tag{A1}$$

When m=0, n>0, the baseband harmonic coefficients are as shown in equation (A2).

$$\begin{aligned} C_{0,n}(h_1) &= \frac{U_{\mathrm{dc}}}{2\pi^2}\int_{-\pi}^{\pi}\int_{-\frac{\pi}{2}(1+M\cos y+M_1\cos h_1 y)}^{\frac{\pi}{2}(1+M\cos y+M_1\cos h_1 y)} e^{jny}\,dx\,dy \\ &= \frac{U_{\mathrm{dc}}}{2\pi}\int_{-\pi}^{\pi}(1+M\cos y+M_1\cos h_1 y)e^{jny}\,dy \\ &= \frac{U_{\mathrm{dc}}}{2\pi}\int_{-\pi}^{\pi}\left\{\begin{array}{l}[e^{jny}+\dfrac{M}{2}(e^{j(n+1)y}+e^{j(n-1)y}) \\ +\dfrac{M_1}{2}(e^{j(n+h_1)y}+e^{j(n-h_1)y})]\end{array}\right\}dy. \end{aligned} \tag{A2}$$

Only when n=1 or n=h_1, equation (A2) is not 0:

$$\begin{cases} C_{0,1}(h_1) = \dfrac{M}{2}U_{dc} \\ C_{0,h_1}(h_1) = \dfrac{M_1}{2}U_{dc}. \end{cases} \tag{A3}$$

When m>0 the carrier and sideband harmonic coefficients can be deduced by equation (A4), where k and d are positive integer ($1\le k\le\infty$, $1\le d\le\infty$). Thus, one phase leg output voltage expression can be obtained as shown in equation (13).

$$
\begin{aligned}
C_{m,n}(h_1) &= \frac{U_{dc}}{2jm\pi^2}\int_{-\pi}^{\pi}(e^{jny}e^{jm\frac{\pi}{2}}e^{-jm\frac{\pi}{2}M\cos y}e^{jm\frac{\pi}{2}M_1\cos(h_1 y)} - e^{jny}e^{-jm\frac{\pi}{2}}e^{-jm\frac{\pi}{2}M\cos y}e^{-jm\frac{\pi}{2}M_1\cos(h_1 y)})dy \\
&= \frac{U_{dc}}{2jm\pi^2}\int_{-\pi}^{\pi}(e^{jny}\left\{\begin{array}{l} e^{jm\frac{\pi}{2}}[J_0(m\frac{\pi}{2}M)+2\sum_{k=1}^{\infty}j^kJ_k(m\frac{\pi}{2}M)\cos(ky)][J_0(m\frac{\pi}{2}M_1)+2\sum_{d_1=1}^{\infty}j^{d_1}J_{d_1}(m\frac{\pi}{2}M_1)\cos(h_1d_1y)] \\ -e^{-jm\frac{\pi}{2}}[J_0(m\frac{\pi}{2}M)+2\sum_{k=1}^{\infty}j^{-k}J_k(m\frac{\pi}{2}M)\cos(ky)][J_0(m\frac{\pi}{2}M_1)+2\sum_{d_1=1}^{\infty}j^{-d_1}J_{d_1}(m\frac{\pi}{2}M_1)\cos(h_1d_1y)] \end{array}\right\})dy \\
&= \frac{U_{dc}}{m\pi^2}\int_{-\pi}^{\pi}\left\{\begin{array}{l} J_0(m\frac{\pi}{2}M)J_0(m\frac{\pi}{2}M_1)\sin(\frac{\pi}{2}m)e^{jny} \\ +J_0(m\frac{\pi}{2}M_1)\sum_{k=1}^{\infty}J_k(m\frac{\pi}{2}M)\sin[(m+k)\frac{\pi}{2}][e^{j(n+k)y}+e^{j(n-k)y}] \\ +J_0(m\frac{\pi}{2}M)\sum_{d_1=1}^{\infty}J_{d_1}(m\frac{\pi}{2}M_1)\sin[(m+d_1)\frac{\pi}{2}][e^{j(n+h_1d_1)y}+e^{j(n-h_1d_1)y}] \\ +\sum_{k=1}^{\infty}\sum_{d_1=1}^{\infty}J_k(m\frac{\pi}{2}M)J_{d_1}(m\frac{\pi}{2}M_1)\sin[(m+k+d_1)\frac{\pi}{2}][e^{j[n+(k+h_1d_1)]y}+e^{j[n-(k+h_1d_1)]y}] \\ +\sum_{k=1}^{\infty}\sum_{d_1=1}^{\infty}J_k(m\frac{\pi}{2}M)J_{d_1}(m\frac{\pi}{2}M_1)\sin[(m+k+d_1)\frac{\pi}{2}][e^{j[n+(k-h_1d_1)]y}+e^{j[n-(k-h_1d_1)]y}] \end{array}\right\}dy \\
&= \frac{2U_{dc}}{m\pi}\left\{\begin{array}{l} J_0(m\frac{\pi}{2}M_1)J_k(m\frac{\pi}{2}M)\sin[(m+k)\frac{\pi}{2}]|_{k=|n|} \\ +J_0(m\frac{\pi}{2}M)J_{d_1}(m\frac{\pi}{2}M_1)\sin[(m+d_1)\frac{\pi}{2}]|_{h_1d_1=|n|} \\ +\sum J_k(m\frac{\pi}{2}M)J_{d_1}(m\frac{\pi}{2}M_1)\sin[(m+k+d_1)\frac{\pi}{2}]|_{\pm k\pm h_1d_1=|n|} \end{array}\right\}
\end{aligned}
\tag{A4}
$$

The output voltage of one H-bridge converter u_{ab} is given by:

$$
\begin{aligned}
u_{ab} &= u_{an}(\theta_c=0,\theta_o=0)-u_{bn}(\theta_c=0,\theta_o=-\pi) \\
&= MU_{dc}\cos(\omega_o t)+M_1U_{dc}\cos(h_1\omega_o t) \\
&\quad +2\sum_{m=1}^{\infty}\sum_{n=-\infty}^{\infty}C_{m,2n-1}(h_1)\cos[m\omega_c t+(2n-1)\omega_o t].
\end{aligned}
\tag{A5}
$$

If N H-bridge converters are cascaded, the shifted phase of the carrier wave is π/N. Thus, the CHBC output voltage is expressed as equation (A6).

$$
\begin{aligned}
u_c &= \sum_{i=1}^{N}u_{abi} = MNU_{dc}\cos(\omega_o t)+M_1NU_{dc}\cos(h_1\omega_o t) \\
&\quad +2\sum_{i=1}^{N}\sum_{m=1}^{\infty}\sum_{n=-\infty}^{\infty}C_{m,2n-1}(h_1)\cos[m(\omega_c t+\frac{(i-1)\pi}{N})+(2n-1)\omega_o t] \\
&= MNU_{dc}\cos(\omega_o t)+M_1NU_{dc}\cos(h_1\omega_o t) \\
&\quad +2\sum_{m=1}^{\infty}\sum_{n=-\infty}^{\infty}C_{m,2n-1}(h_1)\sum_{i=1}^{N}\left\{\begin{array}{l}\cos\frac{m(i-1)\pi}{N}\cos(m\omega_c t+(2n-1)\omega_o t) \\ -\sin\frac{m(i-1)\pi}{N}\sin(m\omega_c t+(2n-1)\omega_o t)\end{array}\right\} \\
&= MNU_{dc}\cos(\omega_o t)+M_1NU_{dc}\cos(h_1\omega_o t) \\
&\quad +\left\{\begin{array}{l}2\sum_{m=1}^{\infty}\sum_{n=-\infty}^{\infty}C_{m,2n-1}(h_1)(\sum_{i=1}^{N}\cos\frac{m(i-1)\pi}{N})\cos(m\omega_c t+(2n-1)\omega_o t) \\ -2\sum_{m=1}^{\infty}\sum_{n=-\infty}^{\infty}C_{m,2n-1}(h_1)(\sum_{i=1}^{N}\sin\frac{m(i-1)\pi}{N})\sin(m\omega_c t+(2n-1)\omega_o t)\end{array}\right\}.
\end{aligned}
\tag{A6}
$$

APPENDIX B

SPECTRUM COEFFICIENT GENERAL SOLUTION FOR MULTIPLE HARMONIC GENERATION

If the modulating wave includes G harmonics at different frequencies, the harmonic coefficients of one phase leg converter are presented. The DC bias coefficient is given by:

$$C_{0,0}(h_1,h_2...h_G)=U_{\mathrm{dc}}. \tag{B1}$$

The baseband harmonic coefficient is given in equation (B2).

$$C_{0,n}(h_1,h_2...h_G)=\begin{cases}\dfrac{M}{2}U_{\mathrm{dc}},n=1\\ \dfrac{M_k}{2}U_{\mathrm{dc}},n=h_k\\ 0,\ \ n\neq h_k\ and\ n\neq 1\end{cases}. \tag{B2}$$

The sideband and carrier harmonic coefficient is the sum of 2^{1+G} items as shown in equation (B4), since $C_{1+G}^{0}+C_{1+G}^{1}+...+C_{1+G}^{1+G}=2^{1+G}$, where C_{1+G}^{r} is given by (B3):

$$C_{1+G}^{r}=\frac{(1+G)!}{r!(1+G-r)!}. \tag{B3}$$

$$\begin{aligned}
\frac{m\pi}{2U_{\mathrm{dc}}}C_{m,n}(h_1,h_2...h_G)=\ & J_0(m\tfrac{\pi}{2}M_1)J_0(m\tfrac{\pi}{2}M_2)...J_0(m\tfrac{\pi}{2}M_G)\sin(m\tfrac{\pi}{2})|_{0=|n|}\Big\}C_{1+G}^{0}\ item\\
&+J_k(m\tfrac{\pi}{2}M)J_0(m\tfrac{\pi}{2}M_1)J_0(m\tfrac{\pi}{2}M_2)....J_0(m\tfrac{\pi}{2}M_G)\sin[(m+k)\tfrac{\pi}{2}]|_{k=|n|}\\
&+J_0(m\tfrac{\pi}{2}M)J_{d_1}(m\tfrac{\pi}{2}M_1)J_0(m\tfrac{\pi}{2}M_2)....J_0(m\tfrac{\pi}{2}M_G)\sin[(m+d_1)\tfrac{\pi}{2}]|_{h_1d_1=|n|}+...\Big\}C_{1+G}^{1}\ items\\
&+J_0(m\tfrac{\pi}{2}M)J_0(m\tfrac{\pi}{2}M_1)J_0(m\tfrac{\pi}{2}M_2)....J_{d_G}(m\tfrac{\pi}{2}M_G)\sin[(m+d_G)\tfrac{\pi}{2}]|_{h_Gd_G=|n|}\\
&+\sum J_k(m\tfrac{\pi}{2}M)J_{d_1}(m\tfrac{\pi}{2}M_1)J_0(m\tfrac{\pi}{2}M_2)....J_0(m\tfrac{\pi}{2}M_G)\sin[(m+k+d_1)\tfrac{\pi}{2}]|_{\pm k\pm h_1d_1=|n|}+...\\
&+\sum J_k(m\tfrac{\pi}{2}M)J_0(m\tfrac{\pi}{2}M_1)J_0(m\tfrac{\pi}{2}M_2)....J_{d_G}(m\tfrac{\pi}{2}M_G)\sin[(m+k+d_G)\tfrac{\pi}{2}]|_{\pm k\pm h_Gd_G=|n|}\\
&+\sum J_0(m\tfrac{\pi}{2}M)J_{d_1}(m\tfrac{\pi}{2}M_1)J_{d_2}(m\tfrac{\pi}{2}M_2)....J_0(m\tfrac{\pi}{2}M_G)\sin[(m+k+d_1)\tfrac{\pi}{2}]|_{\pm h_1d_1\pm h_2d_2=|n|}+...\\
&+\sum J_0(m\tfrac{\pi}{2}M)J_{d_1}(m\tfrac{\pi}{2}M_1)J_0(m\tfrac{\pi}{2}M_2)....J_{d_G}(m\tfrac{\pi}{2}M_G)\sin[(m+k+d_G)\tfrac{\pi}{2}]|_{\pm h_1d_1\pm h_Gd_G=|n|}+...\\
&+\sum J_0(m\tfrac{\pi}{2}M)J_0(m\tfrac{\pi}{2}M_1)J_0(m\tfrac{\pi}{2}M_2)....J_{d_{G-1}}(m\tfrac{\pi}{2}M_{G-1})J_{d_G}(m\tfrac{\pi}{2}M_G)\sin[(m+d_{G-1}+d_G)\tfrac{\pi}{2}]|_{\pm h_{G-1}d_{G-1}\pm h_Gd_G=|n|}\Big\}C_{1+G}^{2}\ summations\\
&+\sum J_k(m\tfrac{\pi}{2}M)J_{d_1}(m\tfrac{\pi}{2}M_1)J_{d_2}(m\tfrac{\pi}{2}M_2)....J_0(m\tfrac{\pi}{2}M_G)\sin[(m+k+d_1+d_2)\tfrac{\pi}{2}]|_{\pm k\pm h_1d_1\pm h_2d_2=|n|}+...\\
&+\sum J_0(m\tfrac{\pi}{2}M)J_0(m\tfrac{\pi}{2}M_1)J_{d_2}(m\tfrac{\pi}{2}M_2)....J_0(m\tfrac{\pi}{2}M_G)\sin[(m+d_{G-2}+d_{G-1}+d_G)\tfrac{\pi}{2}]|_{\pm h_{G-2}d_{G-2}\pm h_{G-1}d_{G-1}\pm h_Gd_G=|n|}\Big\}C_{1+G}^{3}\ summations\\
&+...\qquad\qquad ...\\
&+\sum J_0(m\tfrac{\pi}{2}M)J_{d_1}(m\tfrac{\pi}{2}M_1)J_{d_2}(m\tfrac{\pi}{2}M_2)....J_{d_G}(m\tfrac{\pi}{2}M_G)\sin[(d_1+...+d_{G-1}+d_G)\tfrac{\pi}{2}]|_{\pm h_1d_1\pm h_2d_2+...\pm h_Gd_G=|n|}+...\\
&+\sum J_k(m\tfrac{\pi}{2}M)J_{d_1}(m\tfrac{\pi}{2}M_1)J_{d_2}(m\tfrac{\pi}{2}M_2)....J_0(m\tfrac{\pi}{2}M_G)\sin[(m+d_1+...+d_{G-1})\tfrac{\pi}{2}]|_{\pm k\pm h_1d_1+...h_{G-1}d_{G-1}=|n|}\Big\}C_{1+G}^{G}\ summations\\
&+\sum J_k(m\tfrac{\pi}{2}M)J_{d_1}(m\tfrac{\pi}{2}M_1)J_{d_2}(m\tfrac{\pi}{2}M_2)....J_{d_G}(m\tfrac{\pi}{2}M_G)\sin[(m+d_1+...+d_{G-1}+d_G)\tfrac{\pi}{2}]|_{\pm k\pm h_1d_1\pm h_2d_2+...\pm h_Gd_G=|n|}\Big\}C_{1+G}^{1+G}\ summations
\end{aligned} \tag{B4}$$

ACKNOWLEDGMENT

This work was supported by the Fundamental Research Funds for the Central Universities (under Grant 2018JBZ101) and the National Key Research and Development Program of China (under Grant 2017YFB1200802).

REFERENCES

[1] K. Song, G. Konstantinou, M. Wu, P. Acuna, R. P. Aguilera, and V. G. Agelidis, "Windowed SHE-PWM of interleaved four-quadrant converters for resonance suppression in traction power supply systems," *IEEE Trans. Power Electron.*, Vol. 32, No. 10, pp. 7870-7881, Oct. 2017.

[2] J. Liu, Q. Yang, and T. Q. Zheng, "Harmonic analysis of traction networks based on the CRH380 series EMUs accident," in *Proc. IEEE ITEC Conf.*, pp. 1-6, Jun. 2012.

[3] H. Cui, W. Song, H. Fang, X. Ge, and X. Feng, "Resonant harmonic elimination pulse width modulation-based high-frequency resonance suppression of high-speed railways," *IET Power Electron.*, Vol. 8, No. 5, pp. 735-742, Oct. 2015.

[4] S. M. M. Gazafrudi, A. T. Langerudy, E. F. Fuchs, and K. Al-Haddad, "Power quality issues in railway electrification: A comprehensive perspective," *IEEE Trans. Ind. Electron.*, Vol. 62, No. 5, pp. 3081-3090, May 2015.

[5] W. Song, S. Jiao, Y. W. Li, J. Wang, and J. Huang, "High-frequency harmonic resonance suppression in high-speed railway through single-phase traction converter with LCL filter," *IEEE Trans. Transport. Electrifoc.*, Vol. 2, No. 3, pp. 347-356, Sept. 2016.

[6] S. Wang, W. Song, and X. Feng, "A novel CBPWM strategy for single-phase three-level NPC rectifiers in electric railway traction," in *Proc. IEEE IFEEC Conf.*, pp. 1-6, Nov. 2015.

[7] V. Smidl, S. Janous, and Z. Peroutka, "Improved stability of dc catenary fed traction drives using two stage predictive control," *IEEE Trans. Ind. Electron.*, Vol. 62, No. 5, pp. 3192-3201, May 2015.

[8] M. Brenna, F. Foiadelli, and D. Zaninelli, "Electromagnetic model of high speed railway lines for power quality studies," *IEEE Trans. Power Syst.*, Vol. 25, No. 3, pp. 1301-1308, Aug. 2010.

[9] A. Dolara, M. Gualdoni, and S. Leva, "Impact of high-voltage primary supply lines in the 2×25 kV 50 Hz railway system on the equivalent impedance at pantograph terminals," *IEEE Trans. Power Del.*, Vol. 27, No. 1, pp. 164-175, Jan. 2012.

[10] B. Gustavsen, "Modal domain-based modeling of parallel transmission lines with emphasis on accurate representation of mutual coupling effects," *IEEE Trans. Power Del.*, Vol. 27, No. 4, pp. 2159-2167, Oct. 2012.

[11] A. Bower, "Review of engineering recommendation G5/4-1 stage 3 connections and higher order harmonics," pp. 1-69, April 2013. Available at https://www.nationalgrid.com/sites/default/files/documents/28636-Meeting%207%20-%20Work%20Package%201%20and%202%20Report%20-%20EATL.pdf, accessed Jan. 5th 2018.

[12] M. J. Bridgeman, R. E. Morrison, and S. B. Tenakoon, "Measurement of harmonic impedance on an LV system utilising power capacitor switching and consequent predictions of capacitor induced harmonic distortion," in *Proc. 8th Int. Conf. Harmonics Qual. Power (ICHQP),* pp. 1141-1145, Oct. 1998.

[13] T. G. Martinich, and J. B. Neilson, "Mitigation of resonance using digital models and direct measurement of harmonic impedances," in *Proc. IEEE Power Eng. Soc. Summer Meet.*, pp. 1069-1074, Jul. 2000.

[14] W. Wang, E. E. Nino, and W. Xu, "Harmonic impedance measurement using a thyristor-controlled short circuit," *Inst. Eng. Technol. Gen., Transm. Distrib.*, Vol. 1, No. 5, pp.707-713, Sept. 2007.

[15] R. Stiegler, J. Meyer, P. Schegner, and D. Chakravorty, "Measurement of network harmonic impedance in presence of electronic equipment," in *Proc. IEEE Int. Workshop Appl. Meas. Power Syst. (AMPS)*, pp.49-54, 2015.

[16] L. Asiminoaei, R. Teodorescu, F. Blaabjerg, and U. Borup, "Implementation and test of an online embedded grid impedance estimation technique for PV inverters," *IEEE Trans. Ind. Electron.*, Vol. 52, No. 4, pp. 1136-1144, Aug. 2005.

[17] L. Asiminoaei, R. Teodorescu, F. Blaabjerg, and U. Borup, "A digital controlled PV-inverter with grid impedance estimation for ENS detection," *IEEE Trans. Power Electron.*, Vol. 20, No. 6, pp. 1480-1490, Nov. 2005.

[18] S. Tan, G. Yang, H. Geng, Q. Lv, and H. Wang, "Investigation of harmonic properties of a typical nonlinear load in an AC power-electronics-based micro-grid," in *Proc. IEEE IFEEC Conf.*, pp. 1-5, Nov. 2015.

[19] R. Petrella, A. Revelant, and P. Stocco, "Advances on inter-harmonic variable-frequency injection-based grid-impedance estimation methods suitable for PV inverters," in *Proc. IEEE ECCE*, *Conf.*, pp. 1173-1179, 2009.

[20] D. Reigosa, F. Briz, C. Blanco, and J. M. Guerrero, "Islanding detection in grid-connected power converters using harmonics due to the non-ideal behavior of the inverter," in *Proc. IEEE Energy Convers. Congr. Expo.*, pp. 2649-2656, 2013.

[21] TopCon TC.ACS technical datasheets. Available at https://www.regatron.com/en/products-topcon/topcon-tc-acs/technical-datasheets, accessed Jan. 5th 2018.

[22] L. Wu and M. Wu, "Single-phase cascaded h-bridge multilevel active power filters in AC electric railway systems," *J. Power Electron.*, Vol. 17, No. 3, pp. 788-797, May 2017.

[23] Q. Liu, M. Wu, J. Zhang, K. Song, and L. Wu, "Resonant frequency identification based on harmonic injection measuring method for traction power supply systems," *IET Power Electron.*, Vol. 11, No. 3, pp. 585-592, Mar. 2018.

[24] X. Cai, Z. Wu, Q. Li, and S. Wang, "An improved phase-shifted carrier pulse width modulation based on the artificial bee colony algorithm for cascaded H-Bridge multilevel inverters," *J. Power Electron.*, Vol. 16, No. 2, pp. 512-521, Mar. 2016.

[25] F. Sasongko, and H. Akagi, "Low-switching-frequency operation of a modular multilevel DSCC converter with phase-shifted rotating-carrier PWM," *IEEE Trans. Power Electron.*, Vol. 32, No. 7, pp. 5058-5069, Jul. 2017.

[26] K. Gnanasambandam, A. K. Rathore, A. Edpuganti, D. Srinivasan, and J. Rodriguez, "Current-fed multilevel converters: An overview of circuit topologies, modulation techniques, and applications," *IEEE Trans. Power Electron.,* Vol. 32, No. 5, pp. 3382-3401, May 2017.

[27] R. Naderi, and A. Rahmati, "Phase-shifted carrier PWM technique for general cascaded inverters," *IEEE Trans. Power Electron.*, Vol. 23, No. 3, pp. 1257-1269, May 2008.

[28] M. F. Moussa, and Y. G. Dessouky, "Selective harmonic elimination in multi-level inverters with series-connected transformers with equal power ratings," *J. Power Electron.*, Vol. 16, No.2, pp. 464-472, Mar. 2016.

[29] J. D. B. Ramirez, J. J. R. Rivas, and E. Peralta-Sanchez, "DSP-based simplified space-vector PWM for a three-level

VSI with experimental validation," *J. Power Electron.*, Vol. 12, No. 2, pp. 285-293, Mar. 2012.
[30] S. R. Bowes and B. M. Bird, "Novel approach to the analysis and synthesis of modulation processes in power convertors," *Proc. Inst. Elect. Eng.*, Vol. 122, No. 5, pp. 507-513, 1975.
[31] S. R. Bowes, "New sinusoidal pulsewidth-modulated invertor," *Proc. Inst. Elect. Eng.*, Vol. 122, No. 11, pp. 1279-1285, 1975.
[32] D. G. Holmes and T. A. Lipo, Pulse Width Modulation for Power Converters: Principles and Practice, 1st ed. Hoboken, NJ, USA: Wiley, 2003.
[33] M. Odavic, M. Sumner, P. Zanchetta, and J. C. Clare, "A theoretical analysis of the harmonic content of PWM waveforms for multiple-frequency modulators," *IEEE Trans. Power Electron.*, Vol. 25, No. 1, pp.131-141, Jan. 2010.
[34] D. J. Kostic, Z. Z. Avramovic, and N. T. Ciric, "A new approach to theoretical analysis of harmonic content of PWM waveforms of single- and multiple-Frequency modulators," *IEEE Trans. Power Electron.*, Vol. 28, No. 10, pp. 4557-467, Oct. 2013.
[35] Z. Ji, J. Zhao, Y. Sun, X. Yao, and Z. Zhu, "Fault-tolerant control of cascaded H-Bridge converters using double zero-sequence voltage injection and DC voltage optimization," *J. Power Electron.*, Vol. 14, No. 5, pp. 946-956, Sep. 2014.
[36] Y. Liu，A. Q. Huang，W. Song，S. Bhattacharya, and G. Tan, "Small-signal model-Based control strategy for balancing individual DC capacitor voltages in cascade multilevel inverter-based STATCOM," *IEEE Trans. Ind. Electron.*, Vol. 56, No. 6, pp. 2259-2269, Jun. 2009.
[37] Y. Li, Y. Wang, and B. Q. Li, "Generalized theory of phase-shifted carrier PWM for cascaded H-bridge converters and modular multilevel converters," *IEEE Trans. Emerg. Sel. Topics Power Electron.*, Vol. 4, No. 2, pp. 589-605, Jun. 2016.
[38] H. Dehbonei, L. Borle, and C.V. Nayar, "A review and a proposal for optimal harmonic mitigation in single-phase pulse width modulation," in *Proc., PEDS*, Vol. 1, pp. 408-414, Oct. 2001.
[39] S. Li, Z. Yang, Q. Li, J. Gong, J. Sun, and X. Zha, "Asymmetrical phase-shifting carrier pulse-width modulation for harmonics suppression in cascaded multilevel converter under unbalanced DC-link voltages," in *Proc. IEEE ECCE Conf.*, pp. 6804-6810, 2015.

Qiujiang Liu was born in Hebei Province, China. He received his B.S. and M.S. degrees in Electrical Engineering from Beijing Jiaotong University, Beijing, China, in 2012 and 2014, respectively, where he is presently working towards his Ph.D. degree in Electrical Engineering. His current research interests include the power quality of electric railways and power electronics in power supply systems.

Mingli Wu was born in Hebei Province, China. He received his B.S. and M.S. degrees in Electrical Engineering from Southwest Jiaotong University, Chengdu, China, in 1993 and 1996, respectively. He received his Ph.D. in Electrical Engineering from Beijing Jiaotong University, Beijing, China, in 2006. Since 2008, he has been a Professor in the School of Electrical Engineering, Beijing Jiaotong University. His current research interestes include the power supply for electric railways, the digital simulation of power systems and electric power quality.

Jing Li was born in Henan Province, China. She received her B.S. degree in Electrical Engineering from North China University of Water Resources and Electric Power, Zhengzhou, China, in 2013; and her M.S. degree from Beijing Jiaotong University, Beijing, China, in 2016, where she is presently working towards her Ph.D. degree in Electrical Engineering. Her current research interests include the power quality of electric railways and power electronics in power supply systems.

Junqi Zhang was born in Guangxi Zhuang Autonomous Region, China. He received his B.S. degree in Electrical Engineering from Beijing Jiaotong University, Beijing, China, in 2013, where he is presently working towards his Ph.D. degree in Electrical Engineering. His current research interests include the power supply for electric railways and the digital simulation of power systems.